

Probing the Superconducting Pairing Potential via Dynamical Coulomb Blockade

Chaofei Liu,¹ Pedro Portugal,² Yi Gao,³ Jie Yang,⁴ Xiuying Zhang,⁴ Jing Lu,^{4,5,6,7} Christian Flindt,² Jian Wang^{1,5,8,9,10,†}

¹*International Center for Quantum Materials, School of Physics, Peking University, Beijing 100871, China*

²*Department of Applied Physics, Aalto University, Aalto 00076, Finland*

³*Center for Quantum Transport and Thermal Energy Science, Jiangsu Key Lab on Opto-Electronic Technology, School of Physics and Technology, Nanjing Normal University, Nanjing 210023, China*

⁴*State Key Laboratory for Mesoscopic Physics and School of Physics, Peking University, Beijing 100871, China*

⁵*Collaborative Innovation Center of Quantum Matter, Beijing 100871, China*

⁶*Beijing Key Laboratory for Magnetoelectric Materials and Devices (BKL-MEMD), Beijing 100871, China*

⁷*Peking University Yangtze Delta Institute of Optoelectronics, Nantong 226000, China*

⁸*CAS Center for Excellence in Topological Quantum Computation, University of Chinese Academy of Sciences, Beijing 100190, China*

⁹*Beijing Academy of Quantum Information Sciences, Beijing 100193, China*

¹⁰*Hefei National Laboratory, Hefei 230088, China*

Abstract.—Coulomb blockade occurs for electrons tunneling into nanoislands because of the quantization of charges. Here, using spectroscopy measurements of nonmagnetic islands grown on a high- T_c superconductor [one-unit-cell (1-UC) FeSe], we employ dynamical Coulomb blockade (DCB) as a tool to probe the nature of Cooper pairing in the superconducting substrate. The tunneling spectra are acquired on single-crystalline Pb nanoislands, and show a clear suppression of the tunneling current around zero bias-voltage, i.e. a gap-like structure. The observed spectral gaps can be attributed to DCB based on our comprehensive investigations, including experiments with finely varying island sizes and calculations of the spectra using the $P(E)$ theory of DCB. Our detailed analysis suggests that the observed DCB can be assigned to the sign-reversing pairing potential for the 1-UC FeSe substrate below the islands. The sign reversal is furthermore reflected in a transition of the superconducting gap of FeSe from a U- to a V-like lineshape as the distance between neighboring doublet islands is decreased, indicating the presence of a nodal-like gap as expected for a sign-reversing superconductor. Our configuration of nonmagnetic nanoislands on a high- T_c superconductor for spectroscopy measurements may serve as a local, spatially sensitive, and tunable probe for detecting the sign-reversing order parameter in unconventional superconductors.

One-unit-cell (1-UC) FeSe/SrTiO₃ has received increasing attention in recent years [1]. Compared to bulk FeSe, the significantly enhanced critical temperature (typically $T_c = 55\text{--}65$ K) therein is unusual [2], since superconductivity should be suppressed by fluctuations in low-dimensional systems according to common believes [3,4]. There is no Γ -hole pocket in 1-UC FeSe/SrTiO₃, thus the s_{\pm} -wave pairing based on electron–hole pocket nesting, normally expected in bulk iron-based superconductors [5–10], is unlikely. Theoretically, the pairing symmetry of 1-UC FeSe [11–17] allows both sign-preserving (s_{++} -wave) and sign-reversing pairings (e.g. incipient s_{\pm} , extended s_{\pm} , nodeless d -wave) [12,18]. Therefore, phase-sensitive techniques are called upon to understand its pairing mechanism.

For small tunnel junctions with ultralow capacitances C , Coulomb charging effects and charge quantization combined strongly suppress the tunnel current below the threshold voltage, $V_c = e/2C$, leading to Coulomb blockade [19,20]. A typical STM setup, including the substrate-supported metallic nanocrystals [e.g. Fig. 1(a)], can be modeled as two junctions in describing Coulomb blockade [21], where the nanocrystal/substrate junction (#1) is described by resistance R_1 and capacitance C_1 , in series with the STM tunnel junction (R_2 , C_2) [#2; Fig. 1(b)]. STM-based Coulomb-blockade phenomena have been observed in effective double junctions made of metallic clusters embedded in surface-oxidized metallic substrates [19,20,22]. More recently, such experiments were extended to islands grown on purely metallic or semiconducting substrates (e.g., Cu [23], Al [24], HOPG [23], Si [23,25], InAs [26]). Engineering the electrical contact between nanosized metallic crystals and their supporting substrates is important for designing future electronics. Nevertheless, the Coulomb-blockade effect has been rarely investigated for islands on high- T_c superconductors [27]. Moreover, the interplay between superconducting (SC) correlations and Coulomb interactions is still not well understood.

Dynamical Coulomb blockade (DCB) occurs when single electrons tunneling across a barrier (junction #2) exchange energy with the local high-frequency, high-stray-capacitance ohmic electromagnetic environment (incorporated into junction #1) through emission or absorption of single energy quantum [Fig. 1(c)] [28,29]. In this Letter, we exploit DCB to probe the sign-reversing pairing in a high- T_c superconductor. The STM measurements were performed at 4.2 K

for nonmagnetic (Pb) nanocrystals with volumes V well below the Anderson limit ($V_{\text{Anderson}} \approx 100 \text{ nm}^3$) [30] grown on a high- T_c substrate (1-UC FeSe/SrTiO₃). Based on the $P(E)$ theory of DCB [23,29,32-34], we expect that the low-energy tunneling spectra (dI/dV vs. V) evolve from soft to hard gap, when the Pb/FeSe contact resistance is increased from $R_1 \approx R_Q$ ($R_Q = h/e^2 \approx 25.8 \text{ k}\Omega$, resistance quantum) to $\approx 100R_Q$ [Fig. 1(d)] (Part SI [35]). Essentially, a typical spectrum for low- R_1 junction shows a soft DCB gap [Fig. 1(e)] [28,29], while the high- R_1 ‘version’ recovers the well-known picture of orthodox Coulomb blockade (OCB) instead with a staircase-flanked hard gap [Fig. 1(f)] [36], whose Coulomb-gapped low-energy spectral segment remains robustly captured by the $P(E)$ theory of DCB in high- R_1 limit [Fig. 1(d)].

Notably, the high- T_c 1-UC FeSe is chosen because of its large, tunnel-barrier-type SC gap (10–20 meV [12]) for the contact to metallic Pb islands. Based on the selection rules for Bogoliubov quasiparticles [37], as the non-magnetic scatterer [38], Pb selectively depairs the sign-reversing pairings (e.g. s_{\pm} , d -wave) with induced intragap excitations, but keeps the sign-preserving pairing (s -wave). If sign-reversing s_{\pm} or d -wave pairing dominates in FeSe, the SC gap will be filled with Pb-induced intragap states [inset, Fig. 1(e); termed ‘gap-filled’ case], lowering the barrier. Thus, the electrical Pb nanoisland/FeSe substrate contact could be as low as $R_1 \approx R_Q$ [23], which would give DCB tunneling spectra [Fig. 1(e)]. Yet, if a sign-preserving s -wave pairing dominates, the FeSe substrate should remain fully gapped [inset, Fig. 1(f); ‘gap-reserved’ case] with a large barrier resistance to Pb island, leading to $R_1 \gg R_Q$ [26,39]. Then, the spectrum for tunneling into the Pb island should show OCB accompanied by Coulomb-staircase features [Fig. 1(f)].

Concrete values of R_1 can be determined quantitatively by calculating the transmission spectrum $\tau(E)$ of an experiment-based Pb/FeSe structure (see Methods [35]). In the ‘normal’ (i.e. non-SC) state of Pb/1-UC FeSe, the density-of-states (DoS) spectrum shows metallic and partly gapped behaviors near Fermi level E_F and at -64 meV , respectively [right inset, Fig. 1(g)], which are adopted to simulate separately the situations towards gap-filled and gap-reserved limits. Figure 1(g) plots the calculated full-energy transmission, where the left inset presents the zoom-in of low-energy part with the energy range comparable as measured. Near the gap-filled limit, i.e. at E_F , $\tau = 0.34$, yielding $R_1 = R_Q/\tau \approx 2.9R_Q$, satisfying $R_1 \approx R_Q$; similarly, near the gap-reserved limit, $\tau = 0.085$, yielding $R_1 = R_Q/\tau \approx 11.8R_Q$, indicating $R_1 \gg R_Q$. Consistently, the dominating transmission channel shows decreased tunneling probability in the gap-reserved case, as reflected in its suppressed wavefunctions transmitted into the FeSe layer [Fig. 1(i)] compared to the gap-filled situation [Fig. 1(h)]. In brief, by investigating the electrical contact between nonmagnetic islands and SC substrate based on the Coulomb-blockade phenomena, we can probe the pairing scenario for the SC substrate underneath.

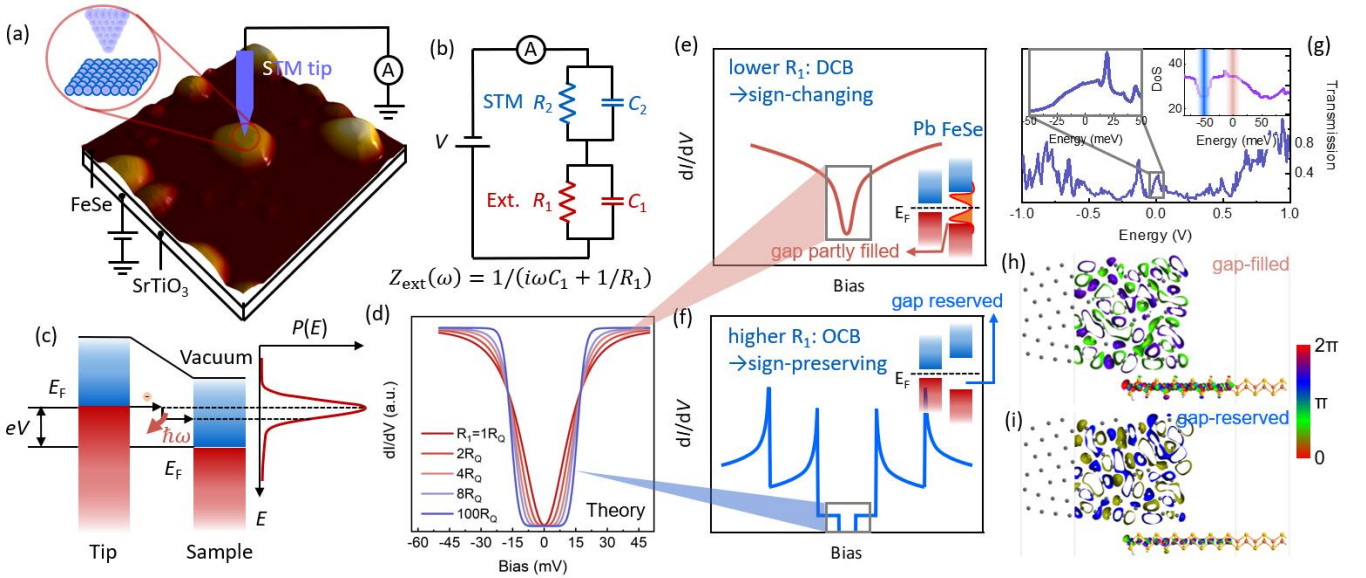


FIG. 1. (a) Schematic of the STM apparatus, showing electrons tunneling into the Pb nanocrystals grown on 1-UC FeSe/SrTiO₃. (b) Equivalent electrical circuit for the STM setup in (a). Z_{ext} , external impedance. (c) Energy diagram of STM electrons tunneling in DCB scenario. The tunneling electron interacts with the local electromagnetic environment via emitting or absorbing energy quantum $E = \hbar\omega$ with a probability given by $P(E)$ function. (d) Examples of dI/dV spectra for different

R_1 calculated using the $P(E)$ theory of DCB [23]. (e,f) Schematic illustrations of DCB and OCB spectra, where the latter is accompanied by Coulomb staircase. These two kinds of Coulomb-blockade phenomena exhibit different low-energy gaps (boxes), highlighting the low- and high- R_1 contacts, respectively, based on the comparison with $R_1=R_Q$ and $=100R_Q$ spectra in (d). A sign-reversing (-preserving) pairing corresponds to the lower (higher) R_1 due to the presence (absence) of intragap states (insets). (g) Calculated full-energy transmission spectrum within $[-1,1]$ eV for a Pb/FeSe structure. Insets, low-energy transmission and DoS spectra. (h,i) Wavefunctions, imprinted on the Pb/FeSe junction, of the dominating eigen-transmission channels for eigen-energies at E_F and -64 meV, which are near the gap-filled and gap-reserved limits, respectively.

Our metallic Pb nanocrystals were prepared *in situ* by depositing Pb on a high-quality 1-UC FeSe/SrTiO₃ (Fig. S1) in a MBE system (see Methods [35]). Single-crystalline Pb nanocrystals, or nanoislands, formed with straight edges, flat tops, and hexagonal shapes, indicating an exposed $[111]$ -oriented structure [Fig. 2(a); Fig. S2 [35]]. Compared with the Pb nanocrystals previously grown on Si(111) [23,25,40], SiC [41], or metallic substrates (Cu, Ag [23]), our Pb islands show particularly well-defined hexagonal shapes, illustrating their high crystalline quality. The Pb nanoislands have lateral sizes of $2L=3-9$ nm (L , side length of hexagon), and thicknesses of $H=2-7$ monolayers (ML; 1 ML=0.286 nm) [Fig. 2(b)]. Using $V = \frac{3\sqrt{3}}{2}L^2H$ for a hexagonal prism, we found volumes in the range $V=4-100$ nm³, corresponding to $0.04V_{\text{Anderson}}-1V_{\text{Anderson}}$. Thus, we obtained a high- T_c substrate supporting well-isolated nonmagnetic nanocrystals with volumes deep in the Anderson limit.

To examine which type of Coulomb blockade is present, we conducted systematic tunneling-spectroscopy measurements on the FeSe-supported Pb nanocrystals. In the dI/dV spectra, a soft gap of ~ 5 meV, which is usually uniform in space within each nanocrystal (Fig. S3 [35]), appears around zero bias with a strong tunnel-current suppression [Figs. 2(c)–2(d)]. Evidently, despite the differences between individual Pb nanocrystals, the soft tunneling gap is reproducibly detected, although sometimes accompanied by irregular spectral features beyond the gap because of the difference of nanocrystals in size and their local environments. Given a 7.2-K T_c for bulk Pb, our soft gap detected at 4.2 K resembles the signature of SC gap, either intrinsic to Pb nanocrystals or induced by proximity effect from FeSe. However, such possibility can be excluded: i) The Pb islands on 1-UC FeSe here are deep below Anderson limit, where superconductivity is quenched [26,42,43]. ii) The majority of Pb-islands dI/dV spectra show no SC coherence peaks flanking the gap. iii) The gap suppression as increasing size [Fig. 3(a), discussed later] is opposite to the behavior as expected for superconductivity. iv) As crossing the Pb island/FeSe edge, the spectral lineshape shows a sharp transition [Fig. 2(f)], rather than a continuous evolution expected for proximity-induced superconductivity.

Instead, we associate the soft gap to DCB effects occurring in double tunnel junctions with relatively low electrical contact (R_1) and high capacitances (C_1) for junction #1 [21,23,24,44], here formed between Pb nanoislands and FeSe substrate. We further performed control experiments with Pb nanoislands grown directly on SrTiO₃ (i.e. without the FeSe layer), yielding a large- R_1 contact barrier (Part SIII [35]), where we indeed found OCB, instead of DCB occurring in the lower-contact Pb/FeSe junctions. Based on the above arguments about the pairing probe, the observation of DCB indicates a sign-reversing pairing of 1-UC FeSe substrate, which is also in line with earlier observations [16,38,45] and the cooperative-pairing conjecture [46].

We also investigated the spectral properties of FeSe substrate in the immediate vicinity of Pb nanocrystals. The results show that the fully gapped, spatially homogeneous SC spectrum in the FeSe substrate remains nearly unchanged independently of however close to the Pb islands [Figs. 2(e)–2(f)]. As the STM tip crosses the Pb-nanocrystal edges, the spectra abruptly turn into soft DCB gaps with a finite zero-bias differential conductance (dI/dV) [Figs. 2(f)–2(h)]. At large bias voltages, e.g., at -30 mV, the spectra with and without the Pb islands are also strikingly different, similarly showing a sharp change [Fig. 2(g)]. The full spectral structure in space is clearly seen in the zero-bias dI/dV map for the Pb nanocrystal [Fig. 2(i)]. Evidently, the finite island conductance (light red) sharply contrasts with the vanishing FeSe conductance (gray). The well-defined conductance hexagon, corresponding to the Pb-nanocrystal profile, illustrates how the spectra alter abruptly. The highly localized nature of DCB spectrum on the nanocrystal region highlights its prospect in probing the SC pairing with nanoscale sensitivity.

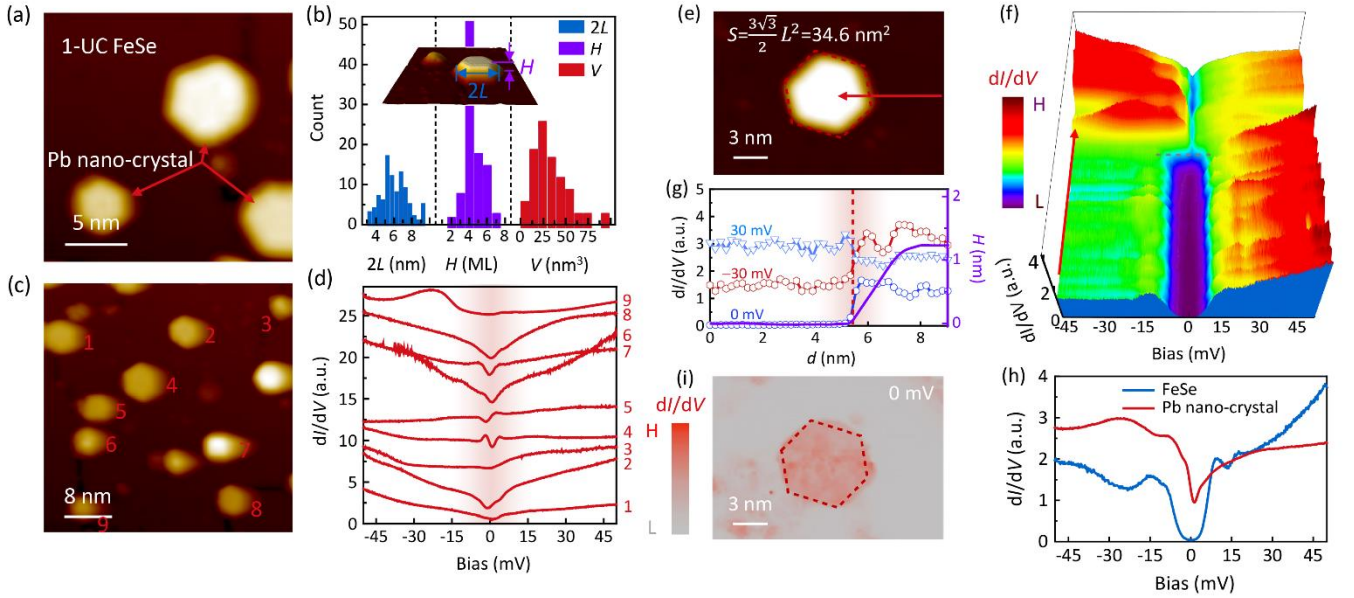


FIG. 2. (a) STM image of Pb nanocrystals on 1-UC FeSe/SrTiO₃(001). (b) Distribution of the lateral size $2L$, height H (inset), and volume V (assuming $V = \frac{3\sqrt{3}}{2}L^2H$) of Pb nanocrystals. (c,d) Numbered Pb nanocrystals and associated tunneling spectra. (e,f) STM image of a Pb nanocrystal, and tunneling spectra measured along the arrow-indicated path therein. See Figs. S6–S8 [35] for edge-crossing spectral-evolution data likewise. (g) Height H profiles and related dI/dV at selected biases (0, -30 and 30 mV) along the same path. d , distance. (h) Tunneling spectra taken on the Pb nanocrystal and directly on the FeSe substrate, showing DCB and SC gaps, respectively. (i) Zero-bias dI/dV map measured for the Pb nanocrystal in (e). Dashed hexagons, Pb-nanocrystal edges. See Part SV [35] for reproduced DCB gaps with high spatial sensitivity.

Independent evidence for DCB is provided by the dependence of soft gap on nanocrystal's surface area. The Coulomb-blockade threshold, $V_c = e/2C$, where the double junction's capacitance with nanocrystal surface area S reads $C = \epsilon_0\epsilon_r S/\delta$ (δ , effective junction thickness), suggests that with increasing S , the DCB gap size should decrease [20]. In Fig. 3(a), we present dI/dV spectra for more than 50 nanocrystals with increasing S . These results show that, despite the spectral fluctuations, the gap width (blue region) generally becomes smaller as the island size S increases, which is consistent with DCB description. To further provide quantitative evidence for DCB, we calculated the tunneling spectra using the $P(E)$ theory of DCB with R_1 and C_1 as fitting parameters [23]. The calculated spectra for the measured data capture the statistical dependence of Coulomb gaps on the island sizes [Fig. 3(b)] and the detailed spectral lineshapes [Fig. 3(c)] observed experimentally. They also yield reasonable values of resistances and capacitances for electrical contacts. Specifically, the obtained average capacitance between Pb islands and FeSe (i.e. $\overline{C_1} = 14.2$ aF) dominates over the capacitance between islands and STM tip ($C_2 \lesssim 1$ aF) [23], and the resistance R_1 spans a range of $\sim 0.05R_Q$ – $1.5R_Q$ corresponding to the expected low-impedance regime [47].

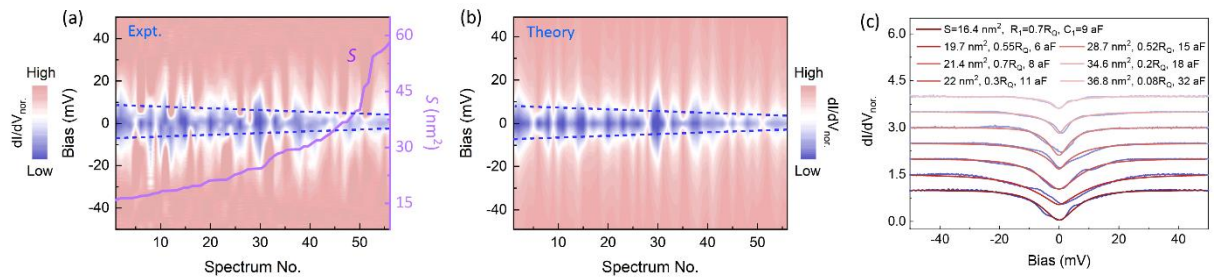


FIG. 3. (a,b) Measured and associated $P(E)$ -theory-calculated [23] DCB spectra for 56 Pb islands. The data are normalized (Part SVI [35]) and ordered by the islands' surface area, $S (= \frac{3\sqrt{3}}{2}L^2)$, which is plotted as a purple line in (a). (c) Comparison of experiment and theory for a few selected tunneling spectra (blue lines, experiment; red lines, theory).

The DCB-revealed gap-sign reversal can also be observed from an inverse effect of the Pb nanocrystals on the SC spectral lineshape of FeSe substrate. The sign-reversing pairing would yield a V-shaped dI/dV spectrum [51] when

nodal lines (i.e. the collection of zero-gap criticality) cross the Fermi surface [52], otherwise remain nodeless, U-gapped. In our experiment, the spectra taken along an ‘open’ trajectory, e.g. the red-arrow-marked one in Fig. 4(a), show a reserved U-like lineshape as normally expected for 1-UC FeSe [Fig. 4(d)]. However, for the trajectory between two adjacent Pb nanocrystals, the spectra become V-shaped with enhanced low-energy quasiparticle excitations [Figs. 4(b)–4(c)]. Based on further statistics over 24 sets of doublet Pb islands, as nanocrystal–nanocrystal distance d_Δ is decreased, the U-gapped SC spectra collected in-between indeed gradually evolve into V-like [Fig. 4(e)]. To quantify the evolution, we fit the low-energy ($|V| \lesssim 10$ mV) spectral parts using an empirical power law, $dI/dV \propto |V|^\alpha$ [inset, Fig. 4(f)] [53]. The extracted d_Δ -dependent α shows a transition to hard-gap opening at $d_\Delta \gtrsim 3.2$ nm [Fig. 4(f)]. Such a ‘nodal transition’ implies that a nodal-gap structure can exist in 1-UC FeSe/SrTiO₃ in specific situations, which supports a sign-reversing gap scenario as suggested by our DCB results.

We now discuss the origin of the U–V-shaped transition. The V gap appearing only for sufficiently adjacent doublet nanoislands suggests that, the scattering potential enhanced at the exposed FeSe region in-between due to superposition is responsible, which modifies E_F to an extent such that it crosses the nodal line to trigger the nodal transition. (For discussions about other possibilities, see Part SVIII [35].) Essentially, the Pb nanoisland can be regarded as a finite-size ‘impurity’ yet with stronger scattering potential given its nature as an ensemble of scatterers [37,54]. Thus, to substantiate the assumption, we calculated the DoS spectra at the middle site of two nonmagnetic impurities with different distances N_Δ [Fig. 4(g)] under various pairing scenarios. Calculations of band structures and pairing-gap function of 1-UC FeSe/SrTiO₃ are based on a previously proposed 2D tight-binding model [55,56] (see Methods in Ref. [38]). The impurity Hamiltonian can be written as $H_{\text{imp}} = \sum_J \sum_{\alpha,\beta=1}^2 (V_{p,\alpha\beta}^J + V_{m,\alpha\beta}^J) c_{R_J A \alpha \uparrow}^\dagger c_{R_J A \beta \uparrow} + (V_{p,\alpha\beta}^J - V_{m,\alpha\beta}^J) c_{R_J A \alpha \downarrow}^\dagger c_{R_J A \beta \downarrow}$. Here, J ($=1, 2$) is the index of impurities located at the Fe atom of sublattice A in the 2-Fe unit cell, with the impurity-site coordinates denoted as \mathbf{R}_J , and $V_{p,\alpha\beta}^J$ is the strength of the potential (nonmagnetic) scattering [intra- ($\alpha = \beta$) or interorbital ($\alpha \neq \beta$)] for the impurity (assuming $V_{p,\alpha\beta}^1 = V_{p,\alpha\beta}^2$).

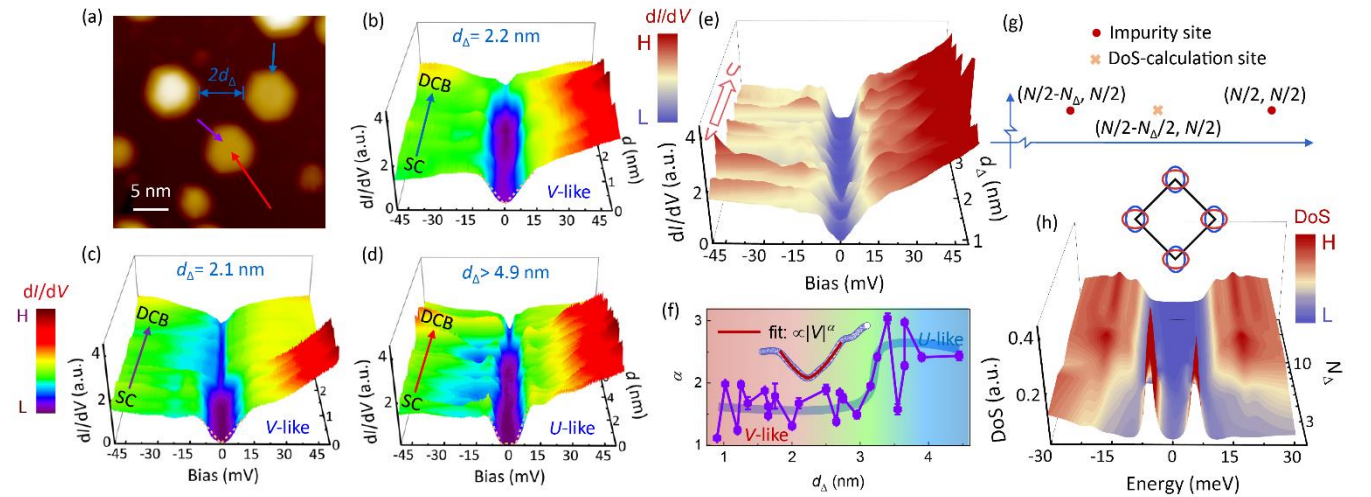


FIG. 4. (a) STM image of Pb nanoislands. d_Δ , half inter-island distance. (b–d) Tunneling spectra taken along the arrows in (a). For more examples of similar phenomena, see Part SVII [35]. (e) Lineshape evolution of SC spectra taken at the middle points of 24 sets of doublet islands as a function of d_Δ . (f) Summary of d_Δ -dependent spectral lineshape, quantified by the exponent α as determined from the fit exemplified in the top-left inset. (g) Schematic showing the DoS-calculation site in the middle of two nonmagnetic impurities at the Fe atom of sublattice A, with the location sites $\mathbf{R}_J = (N/2 - N_\Delta, N/2)$ and $\mathbf{R}_{J'} = (N/2, N/2)$. (h) Calculated ‘middle-site’ DoS in nodeless d -wave pairing scenario for various inter-impurity distances N_Δ . Inset, Fermi-surface topology in folded Brillouin zones. $V_{p,11} = V_{p,22} = 1700$ meV, $V_{p,12} = V_{p,21} = 1300$ meV.

The simulated ‘middle-site’ spectrum, exemplified under nodeless d -wave pairing, appears gap-filled by impurity bound states, and as observed in experiments, turns towards V-shaped (although not ideally) when significantly

decreasing N_Δ [Fig. 4(h)], where enhanced scattering potential is expected. For other pairing scenarios, at sufficiently small $N_\Delta=2$, the simulated spectrum remains U-gapped under isotropic s - and hidden s_\pm -wave pairings, while gets V-like under extended s_\pm -wave pairing (Part SIX [35]). These coincide with the fact that, among the four pairing candidates, sign reversal *near* E_F occurs only in extended s_\pm - and nodeless d -wave pairings, further supporting the spectral U–V crossover taken as the signature of sign-reversing pairing. The induced V-gap transition, combined with the Coulomb blockade, consistently offers a route to determine whether the nodal lines, or sign-reversing pairing, exist in a large-gap U-shaped superconductor. The Coulomb blockade for nonmagnetic islands can be extended on flourishing superconductor substrates, and generalized as a generic phase-sensitive method for probing SC order parameter.

Acknowledgements.—The authors acknowledge assistance from Linqiang Xu in the quantum-transport calculations. Funding: This work was financially supported by National Natural Science Foundation of China (No.11888101), National Key R&D Program of China (No. 2018YFA0305604), Strategic Priority Research Program of Chinese Academy of Sciences (No. XDB28000000), and Innovation Program for Quantum Science and Technology (No. 2021ZD0302403). We also acknowledge support from Academy of Finland through the Finnish Centre of Excellence in Quantum Technology (No. 312057 and No. 312299).

[†]jianwangphysics@pku.edu.cn

- [1] Z. Wang, C. Liu, Y. Liu, and J. Wang, High-temperature superconductivity in one-unit-cell FeSe films, *J. Phys.: Condens. Matter* **29**, 153001 (2017).
- [2] R. M. Fernandes, A. I. Coldea, H. Ding, I. R. Fisher, P. Hirschfeld, and G. Kotliar, Iron pnictides and chalcogenides: a new paradigm for superconductivity, *Nature* **601**, 35 (2022).
- [3] P. C. Hohenberg, Existence of long-range order in one and two dimensions, *Phys. Rev.* **158**, 383 (1967).
- [4] N. D. Mermin and H. Wagner, Absence of ferromagnetism or antiferromagnetism in one- or two-dimensional isotropic Heisenberg models, *Phys. Rev. Lett.* **17**, 1133 (1966).
- [5] X. Chen, P. Dai, D. Feng, T. Xiang, and F.-C. Zhang, Iron-based high transition temperature superconductors, *Natl. Sci. Rev.* **1**, 371 (2014).
- [6] S. Haindl, M. Kidszun, S. Oswald, C. Hess, B. Büchner, S. Kölling, L. Wilde, T. Thersleff, V. Yurchenko, and M. Jourdan, Thin film growth of Fe-based superconductors: from fundamental properties to functional devices. A comparative review, *Rep. Prog. Phys.* **77**, 046502 (2014).
- [7] Q. Si, R. Yu, and E. Abrahams, High-temperature superconductivity in iron pnictides and chalcogenides, *Nat. Rev. Mater.* **1**, 1 (2016).
- [8] Z. Wang, H. Yang, D. Fang, B. Shen, Q.-H. Wang, L. Shan, C. Zhang, P. Dai, and H.-H. Wen, Close relationship between superconductivity and the bosonic mode in $\text{Ba}_{0.6}\text{K}_{0.4}\text{Fe}_2\text{As}_2$ and $\text{Na}(\text{Fe}_{0.975}\text{Co}_{0.025})\text{As}$, *Nat. Phys.* **9**, 42 (2013).
- [9] F. Zhang, C. Kane, and E. Mele, Time-reversal-invariant topological superconductivity and Majorana Kramers pairs, *Phys. Rev. Lett.* **111**, 056402 (2013).
- [10] P. O. Sprau, A. Kostin, A. Kreisel, A. E. Böhmer, V. Taufour, P. C. Canfield, S. Mukherjee, P. J. Hirschfeld, B. M. Andersen, and J. C. S. Davis, Discovery of orbital-selective Cooper pairing in FeSe, *Science* **357**, 75 (2017).
- [11] D. Huang and J. E. Hoffman, Monolayer FeSe on SrTiO_3 , *Annu. Rev. Condens. Matter Phys.* **8**, 311 (2017).
- [12] C. Liu and J. Wang, Heterostructural one-unit-cell FeSe/ SrTiO_3 : from high-temperature superconductivity to topological states, *2D Mater.* **7**, 022006 (2020).
- [13] J. Lee, F. Schmitt, R. Moore, S. Johnston, Y.-T. Cui, W. Li, M. Yi, Z. Liu, M. Hashimoto, and Y. Zhang, Interfacial mode coupling as the origin of the enhancement of T_c in FeSe films on SrTiO_3 , *Nature* **515**, 245 (2014).
- [14] Q. Fan, W. H. Zhang, X. Liu, Y. J. Yan, M. Q. Ren, R. Peng, H. C. Xu, B. P. Xie, J. P. Hu, T. Zhang, and D. L. Feng, Plain s -wave superconductivity in single-layer FeSe on SrTiO_3 probed by scanning tunnelling microscopy, *Nat. Phys.* **11**, 946 (2015).
- [15] Y. Zhang, J. J. Lee, R. G. Moore, W. Li, M. Yi, M. Hashimoto, D. H. Lu, T. P. Devereaux, D. H. Lee, and Z. X. Shen, Superconducting Gap Anisotropy in Monolayer FeSe Thin Film, *Phys. Rev. Lett.* **117**, 117001 (2016).
- [16] H. Zhang, Z. Ge, M. Weinert, and L. Li, Sign changing pairing in single layer FeSe/ SrTiO_3 revealed by nonmagnetic

- impurity bound states, *Commun. Phys.* **3**, 1 (2020).
- [17] C. Liu, A. Kreisel, S. Zhong, Y. Li, B. M. Andersen, P. Hirschfeld, and J. Wang, Orbital-Selective High-Temperature Cooper Pairing Developed in the Two-Dimensional Limit, *Nano Lett.* **22**, 3245 (2022).
- [18] A. Kreisel, P. J. Hirschfeld, and B. M. Andersen, On the Remarkable Superconductivity of FeSe and Its Close Cousins, *Symmetry* **12**, 1402 (2020).
- [19] I. Giaever and H. R. Zeller, Superconductivity of small tin particles measured by tunneling, *Phys. Rev. Lett.* **20**, 1504 (1968).
- [20] H. Zeller and I. Giaever, Tunneling, zero-bias anomalies, and small superconductors, *Phys. Rev.* **181**, 789 (1969).
- [21] D. V. Averin and K. K. Likharev, *Mesoscopic Phenomena in Solids* (Elsevier, Amsterdam, 1991).
- [22] J. Lambe and R. Jaklevic, Charge-quantization studies using a tunnel capacitor, *Phys. Rev. Lett.* **22**, 1371 (1969).
- [23] C. Brun, K. H. Müller, I.-P. Hong, F. Patthey, C. Flindt, and W.-D. Schneider, Dynamical Coulomb blockade observed in nanosized electrical contacts, *Phys. Rev. Lett.* **108**, 126802 (2012).
- [24] J. Senkpiel, J. C. Klöckner, M. Etzkorn, S. Dambach, B. Kubala, W. Belzig, A. L. Yeyati, J. C. Cuevas, F. Pauly, and J. Ankerhold, C. R. Ast, Klaus Kern, Dynamical Coulomb blockade as a local probe for quantum transport, *Phys. Rev. Lett.* **124**, 156803 (2020).
- [25] J. Schmeidel, H. Pfnür, and C. Tegenkamp, Coulomb blockade effects in Ag/Si (111): The role of the wetting layer, *Phys. Rev. B* **80**, 115304 (2009).
- [26] S. Vlaic, S. Pons, T. Zhang, A. Assouline, A. Zimmers, C. David, G. Rodary, J.-C. Girard, D. Roditchev, and H. Aubin, Superconducting parity effect across the Anderson limit, *Nat. Commun.* **8**, 14549 (2017).
- [27] B. Rachmilowitz, H. Zhao, Z. Ren, H. Li, K. H. Thomas, J. Marangola, S. Gao, J. Schneeloch, R. Zhong, G. Gu, C. Flindt, and I. Zeljkovic, Coulomb blockade effects in a topological insulator grown on a high- T_c cuprate superconductor, *npj Quant. Mater.* **5**, 1 (2020).
- [28] P. Delsing, K. Likharev, L. S. Kuzmin, and T. Claeson, Effect of high-frequency electrodynamic environment on the single-electron tunneling in ultrasmall junctions, *Phys. Rev. Lett.* **63**, 1180 (1989).
- [29] M. H. Devoret, D. Estève, H. Grabert, G.-L. Ingold, H. Pothier, and C. Urbina, Effect of the electromagnetic environment on the Coulomb blockade in ultrasmall tunnel junctions, *Phys. Rev. Lett.* **64**, 1824 (1990).
- [30] P.W. Anderson conjectured in 1959 that superconductivity in isolated nanoparticles could only exist if $\delta E < \Delta$ [δE , energy spacing (Kubo gap) of quantum-confined levels; Δ , SC gap energy] [31]. The Anderson limit, a transition point where $\delta E = \Delta$, defines a critical size (V_{Anderson}) of superconductor that can be deduced from the size-limited δE via quantum confinement.
- [31] P. W. Anderson, Theory of dirty superconductors, *J. Phys. Chem. Solids* **11**, 26 (1959).
- [32] S. Girvin, L. Glazman, M. Jonson, D. R. Penn, and M. D. Stiles, Quantum fluctuations and the single-junction Coulomb blockade, *Phys. Rev. Lett.* **64**, 3183 (1990).
- [33] G.-L. I. Y. V. Nazarov, in *Single Charge Tunneling* (Plenum, New York, 1992).
- [34] P. Joyez and D. Esteve, Single-electron tunneling at high temperature, *Phys. Rev. Lett.* **56**, 1848 (1997).
- [35] See Supplemental Material for Methods, difference of DCB and OCB, sample characterizations, control experiments, additional DCB data, spectral normalization, more examples of spectral U–V crossover, discussions about other V-gap's origins, and inter-impurity site DoS calculations under various pairing scenarios.
- [36] A. Hanna and M. Tinkham, Variation of the Coulomb staircase in a two-junction system by fractional electron charge, *Phys. Rev. B* **44**, 5919 (1991).
- [37] A. V. Balatsky, I. Vekhter, and J.-X. Zhu, Impurity-induced states in conventional and unconventional superconductors, *Rev. Mod. Phys.* **78**, 373 (2006).
- [38] C. Liu, Z. Wang, Y. Gao, X. Liu, Y. Liu, Q.-H. Wang, and J. Wang, Spectroscopic Imaging of Quasiparticle Bound States Induced by Strong Nonmagnetic Scatterings in One-Unit-Cell FeSe/SrTiO₃, *Phys. Rev. Lett.* **123**, 036801 (2019).
- [39] J. Reiner, A. K. Nayak, A. Tulchinsky, A. Steinbok, T. Koren, N. Morali, R. Batabyal, J.-H. Kang, N. Avraham, and Y. Oreg, Spectroscopic visualization of a robust electronic response of semiconducting nanowires to deposition of superconducting islands, *Phys. Rev. X* **10**, 011002 (2020).
- [40] J.-F. Jia, S.-C. Li, Y.-F. Zhang, and Q.-K. Xue, Quantum size effects induced novel properties in two-dimensional

- electronic systems: Pb thin films on Si(111), *J. Phys. Soc. Jpn.* **76**, 082001 (2007).
- [41] C. Liu, C. Zhao, S. Zhong, C. Chen, Z. Zhang, Y. Jia, and J. Wang, Equally Spaced Quantum States in van der Waals Epitaxy-Grown Nanoislands, *Nano Lett.* **21**, 9285 (2021).
- [42] S. Bose, C. Galande, S. Chockalingam, R. Banerjee, P. Raychaudhuri, and P. Ayyub, Competing effects of surface phonon softening and quantum size effects on the superconducting properties of nanostructured Pb, *J. Phys.: Condens. Matter* **21**, 205702 (2009).
- [43] J. Liu, X. Wu, F. Ming, X. Zhang, K. Wang, B. Wang, and X. Xiao, Size-dependent superconducting state of individual nanosized Pb islands grown on Si(111) by tunneling spectroscopy, *J. Phys.: Condens. Matter* **23**, 265007 (2011).
- [44] L. Serrier-Garcia, J. Cuevas, T. Cren, C. Brun, V. Cherkez, F. Debontridder, D. Fokin, F. Bergeret, and D. Roditchev, Scanning tunneling spectroscopy study of the proximity effect in a disordered two-dimensional metal, *Phys. Rev. Lett.* **110**, 157003 (2013).
- [45] Z. Ge, C. Yan, H. Zhang, D. Agterberg, M. Weinert, and L. Li, Evidence for d-wave superconductivity in single layer FeSe/SrTiO₃ probed by quasiparticle scattering off step edges, *Nano Lett.* **19**, 2497 (2019).
- [46] D.-H. Lee, Routes to high-temperature superconductivity: a lesson from FeSe/SrTiO₃, *Annu. Rev. Condens. Matter Phys.* **9**, 261 (2018).
- [47] There is actually no dielectric insulator deposited between Pb nanocrystals and 1-UC FeSe, thus likely no Schottky barrier existing at their interface. The origin of contact R_1 is rationalized by noting that the Fermi wavelength ($\lambda_F=3.8$ nm [48]) of 1-UC FeSe is comparable with the lateral size of the nanocrystals ($2L=3-9$ nm). Such constriction of wavefunction, in a limited degree, yields suppressed transmission coefficient [49,50], thus the existence of contact resistance R_1 . The scenario is also confined by the fact that R_1 decreases with the area of nanocrystals.
- [48] Z. Li, J.-P. Peng, H.-M. Zhang, C.-L. Song, S.-H. Ji, L. Wang, K. He, X. Chen, Q.-K. Xue, and X.-C. Ma, Visualizing superconductivity in FeSe nanoflakes on SrTiO₃ by scanning tunneling microscopy, *Phys. Rev. B* **91**, 060509 (2015).
- [49] B. Van Wees, H. Van Houten, C. Beenakker, J. G. Williamson, L. Kouwenhoven, D. Van der Marel, and C. Foxon, Quantized conductance of point contacts in a two-dimensional electron gas, *Phys. Rev. Lett.* **60**, 848 (1988).
- [50] C. Pasquier, U. Meirav, F. Williams, D. Glatli, Y. Jin, and B. Etienne, Quantum limitation on Coulomb blockade observed in a 2D electron system, *Phys. Rev. Lett.* **70**, 69 (1993).
- [51] C.-L. Song, Y.-L. Wang, P. Cheng, Y.-P. Jiang, W. Li, T. Zhang, Z. Li, K. He, L. Wang, J.-F. Jia, H.-H. Hung, C. Wu, X. Ma, C. Xi, and Q.-K. Xue, Direct observation of nodes and twofold symmetry in FeSe superconductor, *Science* **332**, 1410 (2011).
- [52] P. Hirschfeld, M. Korshunov, and I. Mazin, Gap symmetry and structure of Fe-based superconductors, *Rep. Prog. Phys.* **74**, 124508 (2011).
- [53] T. Watashige, Y. Tsutsumi, T. Hanaguri, Y. Kohsaka, S. Kasahara, A. Furusaki, M. Sigrist, C. Meingast, T. Wolf, H. v. Löhneysen, T. Shibauchi, and Y. Matsuda, Evidence for Time-Reversal Symmetry Breaking of the Superconducting State near Twin-Boundary Interfaces in FeSe Revealed by Scanning Tunneling Spectroscopy, *Phys. Rev. X* **5**, 031022 (2015).
- [54] M. Mashkooori, A. Moghaddam, M. Hajibabaei, A. M. Black-Schaffer, and F. Parhizgar, Impact of topology on the impurity effects in extended s-wave superconductors with spin-orbit coupling, *Phys. Rev. B* **99**, 014508 (2019).
- [55] Y. Gao, Y. Yu, T. Zhou, H. Huang, and Q.-H. Wang, Hidden sign-changing s-wave superconductivity in monolayer FeSe, *Phys. Rev. B* **94**, 144512 (2016).
- [56] Y. Gao, Y. Yu, T. Zhou, H. Huang, and Q.-H. Wang, Possible spin excitation structure in monolayer FeSe grown on SrTiO₃, *Phys. Rev. B* **96**, 014515 (2017).

METHODS

Sample growth and STM/STS experiments.—The experiments were performed in an ultrahigh-vacuum (5×10^{-11} – 2×10^{-10} mbar) MBE–STM combined system. The Nb-doped (0.7%-w.t.) SrTiO₃ substrate is prepared by a Se-flux-etching method [1]. The 1-UC FeSe film was epitaxially grown on Nb-doped SrTiO₃ following the well-established recipe [2]. By evaporating Pb from a standard Knudsen cell in the MBE chamber, the high-purity Pb atoms were deposited on FeSe (SrTiO₃) surface kept at room temperature, at a rate of 0.17 ML/min. Via Volmer–Weber, i.e., island mode [3], the growth of Pb on 1-UC FeSe proceeds directly with the crystallization of individual nanoislands, without the first formation of 1–2 ML Pb wetting layer [4]. All the STM topographic images and tunneling spectra were measured at 4.2 K. For STM measurements, a bias voltage was equivalently applied to the sample. A mechanically sharpened polycrystalline PtIr tip was used throughout the experiments. The topographic images were obtained in a constant-current mode, with typical tunneling-junction setpoints: $V_s = 0.2$ – 0.5 V, $I_t = 0.2$ – 2.5 nA. The tunneling spectra were acquired at $V_s = 40$ mV, $I_t = 2.5$ nA using the standard lock-in technique with a bias modulation of 1 mV at 1.7699 kHz.

Quantum-transport calculations.—The 1-UC FeSe is firstly fully optimized with the lattice parameter converged at $a_0=b_0=3.70$ Å. The 1-UC FeSe and Pb metal interface system is then constructed through putting 1-UC FeSe on one side of the Pb metal surface, and the interlayer distance between the two surface is initially set to be about 3.2 Å. The Pb metal surface is simulated with a six Pb atom layers slab along the $\langle 111 \rangle$ direction. The lattices of the Pb slab are changed to match a 3×2 1-UC FeSe supercell with the mismatch of 4.6%, as the Pb island is later grown onto 1-UC FeSe. The lattice parameters of the interface system are kept during the geometrical optimization process. A vacuum buffer space is set to be at least 12 Å to avoid spurious interactions.

The geometry optimization and electronic property calculation are performed within the Vienna *ab initio* simulation package (VASP). The plane-wave basis set with the cut-off energy of 600 eV and projector augmented wave (PAW) pseudopotential is employed. The exchange-correlation functional is generalized gradient approximation (GGA) with the Perdew–Burke–Ernzerhof (PBE) parametrization. A fine k -mesh density of 0.02 Å⁻¹ under the Monkhorst–Pack method is sampled in the Brillouin zone. The atoms are relaxed until the residual force is less than 0.01 eV Å⁻¹/atom and the total energies converge less than 1×10^{-6} eV/atom.

A two-probe device configuration is built to simulate the transportation process between the 1-UC FeSe and Pb island. The 1-UC FeSe and Pb interface system is used as channel, and the metal Pb and 1-UC FeSe are used as left and right electrode, respectively. The building of the device and transport property calculations are implemented in the Atomistix ToolKit 2020 package, and use nonequilibrium Green’s function (NEGF) method coupled with the DFT. The transmission coefficient $\tau_{k_{\parallel}}(E)$ can be obtained in the irreducible Brillouin zone (IBZ)) by

$$\tau_{k_{\parallel}}(E) = \text{Tr} \left[\Gamma_{k_{\parallel}}^l(E) G_{k_{\parallel}}(E) \Gamma_{k_{\parallel}}^r(E) G_{k_{\parallel}}^{\dagger}(E) \right]$$

where $G_{k_{\parallel}}(E)$ and $G_{k_{\parallel}}^{\dagger}(E)$ are the retarded and advanced Green’s functions, respectively.

$\Gamma_{k_{\parallel}}^{l(r)}(E) = i \left(\sum_{l(r), k_{\parallel}}(E) - \sum_{l(r), k_{\parallel}}^{\dagger}(E) \right)$ represents the level broadening originating from the left and right electrodes in the form of self-energy $\sum_{l(r), k_{\parallel}}(E)$, which reflects the influence of the electrodes on the scattering region. k_{\parallel} is a reciprocal lattice vector point along a surface-parallel direction (orthogonal to the transmission direction) in the IBZ. Double- ζ plus polarization (DZP) basis set is employed, the kinetic-energy cutoff is of 120 Hartree, and the temperature is set at 300 K. The X and Y directions of the device take Neumann and Periodic boundary condition, respectively. The transport Z direction takes a Dirichlet-type boundary condition.

SUPPLEMENTARY TEXT

I. Coulomb Blockade: DCB and OCB Regimes

For Coulomb blockade, due to the quantized electronic-charging effects, electrons only tunnel when the applied voltage bias V can overcome the charging energy, i.e. $e|V| \geq E_c = e^2/2C$, yielding threshold $V_c = e/2C$. Below $|V_c|$, because of the blocked electron accumulation by Coulomb repulsion, tunneling is strongly suppressed. Benefiting from technological advances in nano-fabrication techniques and STM/S, the Coulomb-blockade effect has been explored in elaborate planar or point-contact junctions with ultralow capacitances [5]. These investigations are not only important for understanding the physics of small conductors in low dimensions [6], but also paving the way for a range of electronic applications, such as current standards, electrometry, fast-switching devices, and single-electron memories [7-9].

Two preconditions are crucial for Coulomb blockade [6,10]: i) low temperature, to ensure the charging energy E_c is higher than the thermal energy $k_B T$; ii) sufficiently large tunnel resistance R compared with the quantum resistance R_Q , to suppress the smearing by quantum fluctuations. For the STM-based double junction (island–substrate junction #1 and tip–island junction #2), the tip–island junction resistance R_2 (1 M Ω –1 G Ω ; here $\gtrsim 15$ M Ω for the typical setpoints of our STM) is always significantly larger than R_Q . Based on the semiclassical theory [11-13], and also supported by our calculations via $P(E)$ theory [Fig. 1(d)], the electron-transport behavior through such type of double junction naturally falls into three regimes.

i) When island–substrate junction resistance $R_1 \ll R_Q$, the system is essentially a single junction.

ii) When R_1 is of the order of R_Q , the dynamical Coulomb blockade (DCB) regime is reached. The involved inelastic tunneling therein yields a dip (soft gap) near zero bias.

iii) When $R_1 \gg R_Q$, the regime of orthodox Coulomb blockade (OCB) is entered. For the capacitive situation of our STM-based double junction, where $C_1 > C_2$, the hard Coulomb gap would appear at $\pm e/2C_1$, accompanied by Coulomb staircase with interval e/C_2 , corresponding to whenever an extra electron is accommodated in the central electrode (i.e., the nanoisland, or nanocrystal in our work) [13].

II. STM Characterizations of Pb Nanocrystals on 1-UC FeSe/SrTiO₃

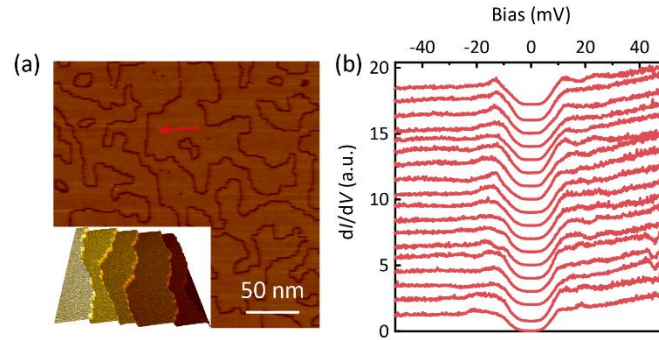


FIG. S1. (a) STM topography of a step-free 1-UC FeSe region. Inset: a large-scale topographic image (500×500 nm²). (b) Spatially resolved tunneling spectra (vertically offset for clarity) taken along the arrow-indicated straight-line trajectory on FeSe surface in (a). As previous reports [14], the spectra show the double-SC-gap feature, characteristic of the multiband superconductivity in 1-UC FeSe. Notably, these spectra taken along the 40-nm-long trajectory is stable in lineshape with negligible change, together with the atomically flat morphology over > 500 nm shown in (a), suggesting the high crystal quality of our 1-UC FeSe sample.

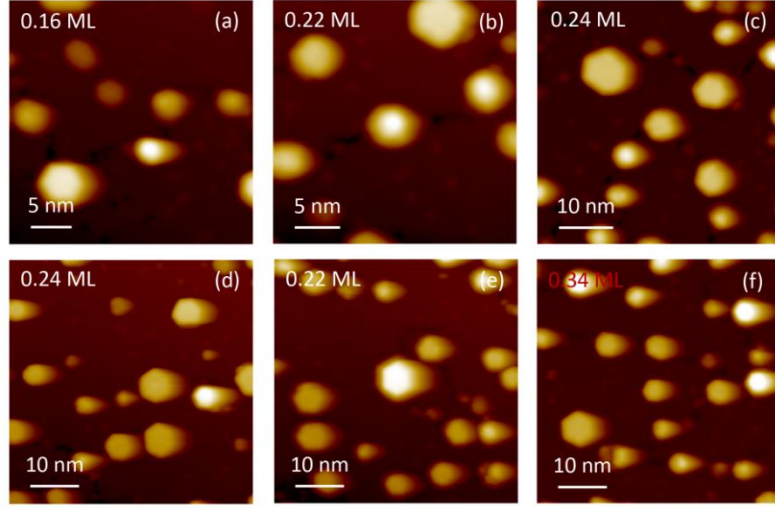


FIG. S2. STM topographic images of Pb nanocrystals with different coverages deposited on 1-UC FeSe. A majority of the Pb nanocrystals reproducibly show well-defined hexagonal shapes with flat top, suggesting their high crystallinity.

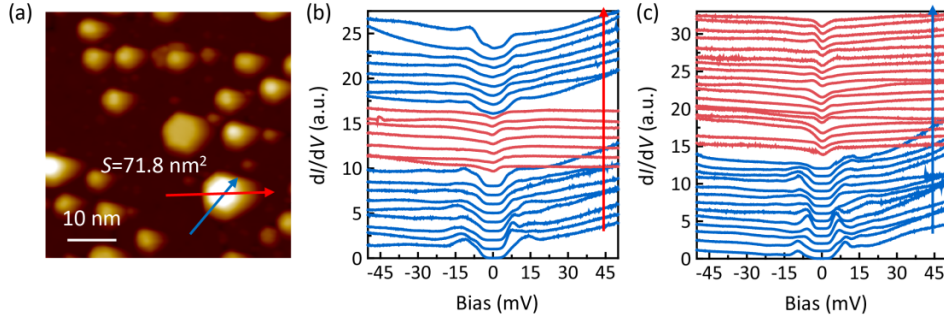


FIG. S3. Spatial homogeneity of the DCB spectra taken on Pb nanocrystals. (a) STM topographic image of Pb nanocrystals on 1-UC FeSe. (b,c) Tunneling spectra (vertically offset for clarity) taken along the arrows in (a), exemplifying nearly unchanged spectral lineshapes of SC gap (blue curves) and DCB gap (red curves) on 1-UC FeSe and Pb nanocrystals, respectively. The blue curves represent the spectra measured on FeSe, and the red ones on Pb islands. The uniform dI/dV spectra in space collected for a given island justify its high crystallinity, which warrants further analysis based a single spectrum for each island.

III. Control Experiments for Revealing Lower-Impedance Contact Between Pb Nanoislands and FeSe Substrate

To check the role of contact resistance (R_1) on Coulomb blockade, control experiments are performed for Pb nanocrystals grown on another substrate, Nb:SrTiO₃ [Figs. S4(a)–S4(b)], a dilutedly doped semiconductor. SrTiO₃, with a large bandgap (2–3 eV [15,16]) even after Nb doping (w.t. 0.7%), supposedly serves as a large barrier. Thus, the contact resistance should be larger than the case of partly intragap-filled FeSe. Tunneling dI/dV spectra are taken at SrTiO₃-supported Pb nanocrystals [Fig. S4(c)] with comparable, or slightly larger size relative to those showing DCB on FeSe ($2L \approx 3\text{--}9$ nm; L is the hexagon side length). The results include that, i) the dI/dV spectrum for a small island with $2L = 8.8$ nm shows discrete Coulomb peaks outside a central hard Coulomb gap near zero voltage; ii) as the size increases (overall $2L \lesssim 22$ nm here), the spectrum evolves into a lineshape showing only the central hard gap flanked by initially developed one or two pairs of Coulomb peaks. These observations in both situations represent the signatures of OCB. The gap consists of Coulomb blockade-gapped features arising due to the island–substrate junction (#1), and is additionally superposed with interaction effect-induced correlation gap in dimension-reduced, ultra-small sized systems due to suppressed Coulomb screening therein, whose contribution is expected to decrease when the size gets larger [17–20], as observed here; while the flanking peaks are related to the tip–island tunnel junction (#2). The bias-asymmetric lineshape for some spectra is attributable to the residual charge Q_0 in the nanocrystals [13]. In contrast, the islands with size comparable with, or larger than the bulk SC coherence length ξ ($\xi_{\text{Pb}} = 83$ nm), still show the well-defined SC spectra as expected (Fig. S5), indicating the OCB signals are indeed reliable.

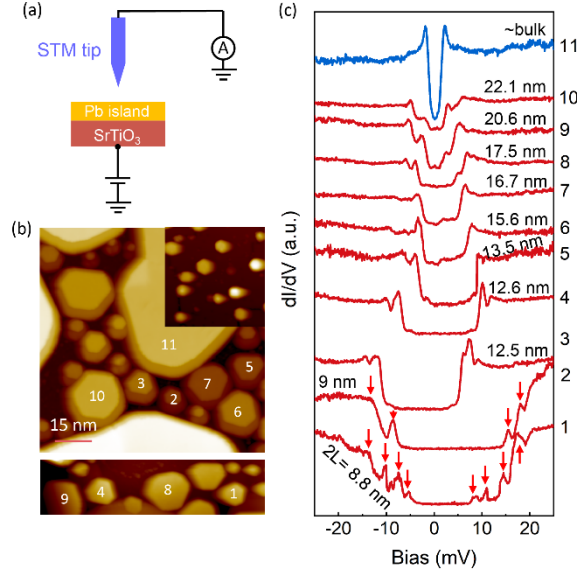


FIG. S4. OCB detected on the Pb nanoislands directly grown on SrTiO₃. (a) Schematic of STM-measured Pb nanoislands/SrTiO₃. (b) STM image of the Pb nanocrystals/SrTiO₃. Inset shows the image of Pb nanocrystals/1-UC FeSe sharing the same scale bar as main panel, for a direct size comparison of islands on different substrates. (c) Tunneling spectra taken on the SrTiO₃-supported Pb nanocrystals [as numbered in (b)] with the size comparable, or a little larger than those on FeSe (except #11, a control spectrum for bulk-like Pb island). The spectra, vertically offset for clarity, are ordered by island size ($2L$) as marked. The discrete peaks, the signatures of Coulomb blockade, are marked by arrows for the bottom spectrum as an example.

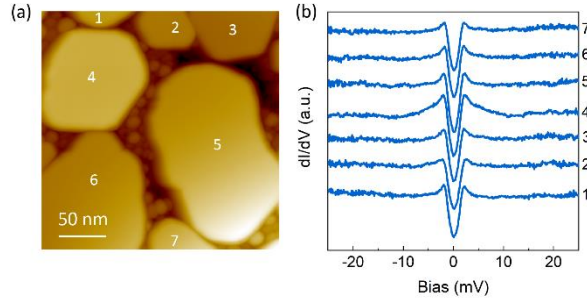


FIG. S5. (a) STM image of larger-sized Pb islands (≥ 50 –100 nm). (b) Tunneling spectra (vertically offset for clarity) taken on the numbered islands in (a), showing SC characteristic.

IV. DCB Gap for Tunneling into Pb Nanocrystals

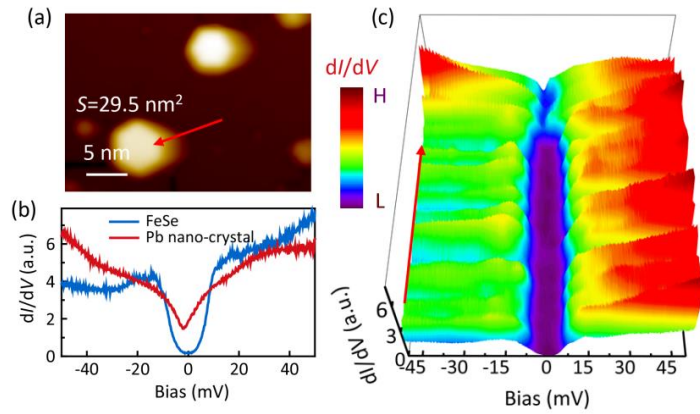


FIG. S6. Additional DCB example #1. (a) STM topographic image of Pb nanocrystals on 1-UC FeSe. (b) Tunneling spectra taken on 1-UC FeSe and Pb nanocrystals, respectively. (c) 3D false-color plot of the tunneling spectra taken along the arrow in (a).

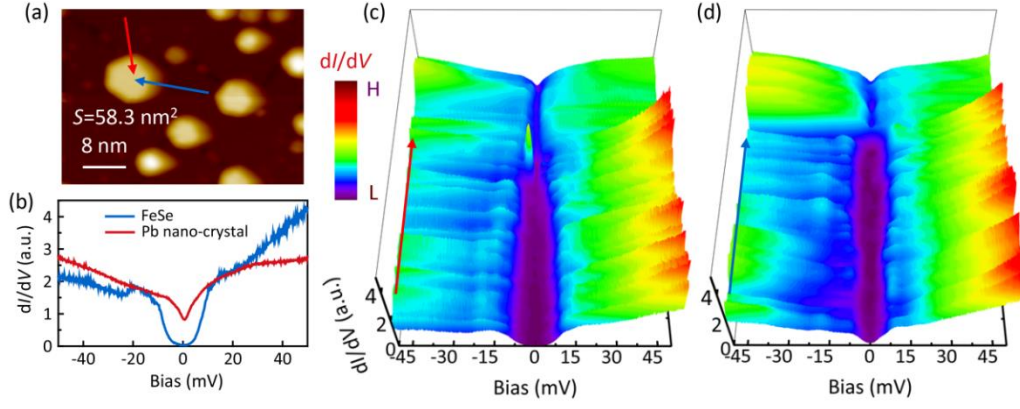


FIG. S7. Additional DCB example #2. (a) STM topographic image of Pb nanocrystals on 1-UC FeSe. (b) Tunneling spectra taken on 1-UC FeSe and Pb nanocrystals, respectively. (c,d) 3D false-color plots of the tunneling spectra taken along the arrows in (a).

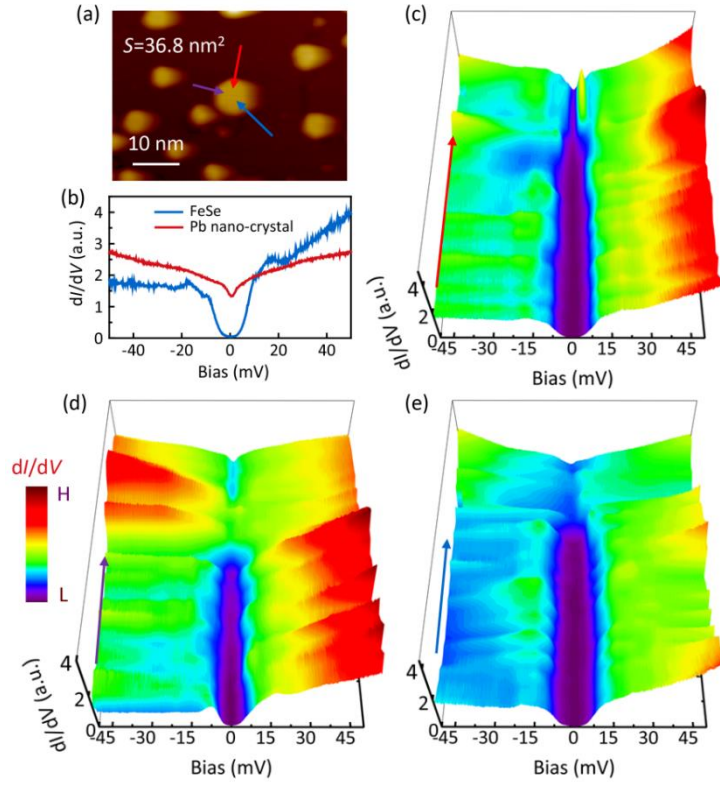


FIG. S8. Additional DCB example #3. (a) STM topographic image of Pb nanocrystals on 1-UC FeSe. (b) Tunneling spectra taken on 1-UC FeSe and Pb nanocrystals, respectively. (c-e) 3D false-color plots of the tunneling spectra taken along the arrows in (a).

V. Sharp Spectral Transition at the Boundary Between FeSe and Pb Nanocrystals

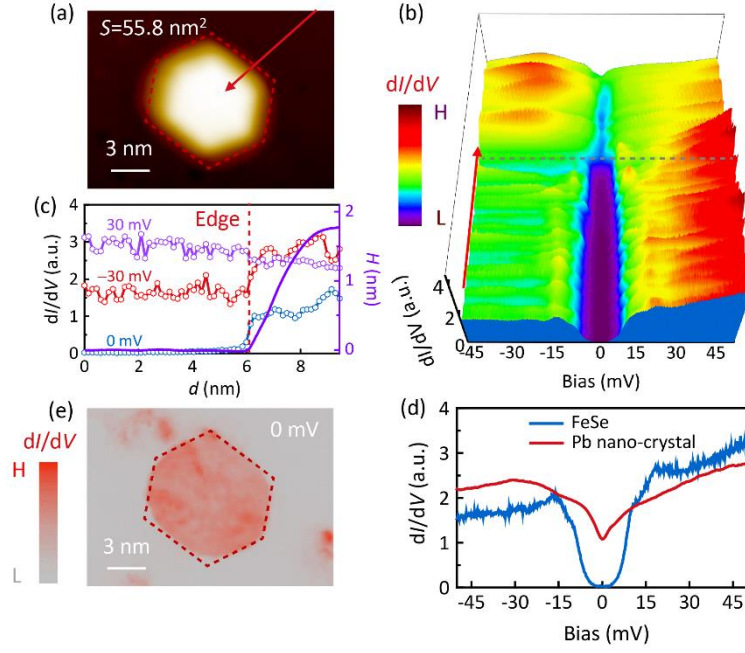


FIG. S9. Additional example of sharp transition of the spectral lineshape across Pb nanocrystals edge. (a) STM topographic image of a Pb nanocrystals. (b) 3D false-color plot of the tunneling spectra taken along the arrow in (a). (c) Differential-conductance $dI/dV(0 \text{ mV}, \pm 30 \text{ mV})$ linecuts and height H profiles across the Pb nanocrystals edge along the arrow in (a). (d) Tunneling spectra taken on 1-UC FeSe and Pb nanocrystals, showing SC gap and DCB gap, respectively. (e) dI/dV map taken at 0 mV for the Pb nanocrystals in (a). The dashed hexagons in (a) and (e) depict the profile of the Pb nanocrystals.

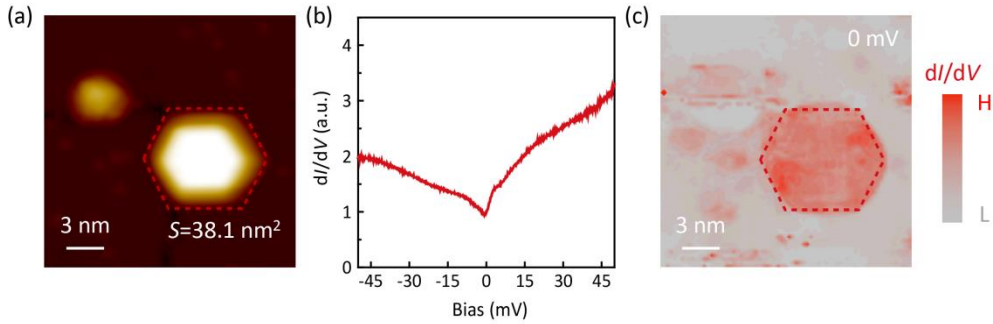


FIG. S10. (a) STM topographic image of a Pb nanocrystals. (b,c) Tunneling spectra and dI/dV map taken at 0 mV for the Pb nanocrystals in (a). The well-preserved, nearly size-unchanged hexagonal shape in $dI/dV(0 \text{ mV})$ map for the Pb nanocrystals suggests the sharp spectral transition at nanocrystals edge.

VI. Normalization of Tunneling Spectra

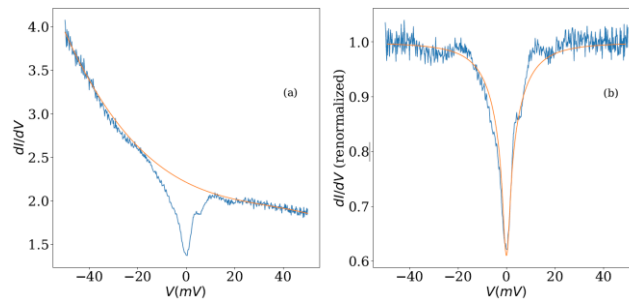


FIG. S11. In (a), we fit the raw tunneling spectrum (blue) with a third-degree polynomial (yellow) for $|V| > 35 \text{ mV}$, and divide the raw spectrum by it. Then, in (b), the normalized spectrum (blue) is fitted according to the DCB model (yellow) [21].

VII. U–V Crossover for SC Lineshape of 1-UC FeSe

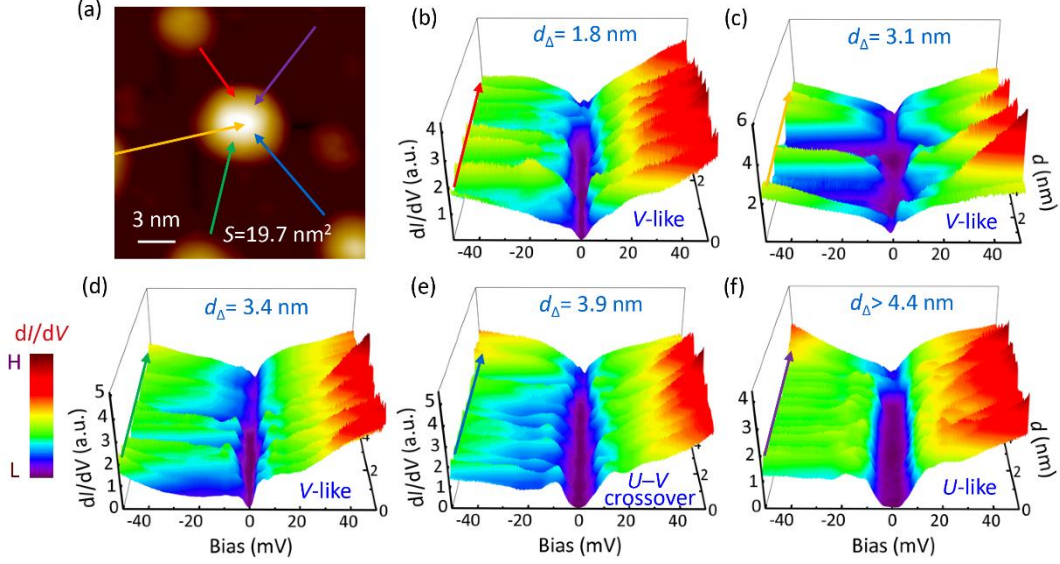


FIG. S12. (a) STM topographic image of Pb nanocrystals. (b–f) 3D false-color plots of the tunneling spectra taken along the arrows in (a). Evidently, as increasing the inter-island distance $2d_\Delta$, U–V crossover occurs for the SC-gap lineshape of 1-UC FeSe.

VIII. Discussions about Other Possibilities as the Origin of V-Shaped Gap in 1-UC FeSe/SrTiO₃

Inverse proximity effect (IPE) of Pb nanocrystals on FeSe, if any, will weaken the superconductivity of FeSe, making the gap be filled with quasiparticle excitations and thus turn V-shaped. Based on the following arguments, the possibility of IPE can be excluded.

- i) The IPE scenario should in principle show no preference and be applicable to both individually isolated and sufficiently close doublet islands, while in experiments the V-gapped spectra only exist in the latter of these two situations.
- ii) FeSe shows no SC proximity effect on Pb islands, which thus likely exert no IPE on FeSe.
- iii) The weakened superconductivity of V shape due to IPE normally yields elevated zero-bias conductance (ZBC). However, in our experiments, the ZBC for V-gapped spectra at $d_\Delta < d_\Delta^c$ (3.2 nm) remains nearly zero and presents no obvious difference from that for U-shaped spectra at $d_\Delta > d_\Delta^c$ (Fig. S13).

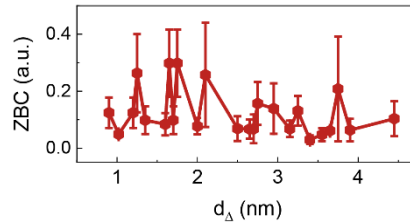


FIG. S13. ZBC as a function of d_Δ . The error bar is determined as half the difference between maximum and minimum ZBC extracted from a set of spectra for a fixed d_Δ .

Suppressed superconductivity in reduced size by quantum confinement can also give the V-shaped gap. Yet, the SC coherence length of 1-UC FeSe is ~ 2 nm [22], smaller than the critical $d_\Delta^c \sim 3.2$ nm where the nodal crossover occurs.

Another candidate physical reason behind can be the decreased chemical potential by quantum confinement. Nonetheless, the decreased Fermi energy due to quantum confinement will shrink the size of electron Fermi pockets at M point, while the possibility of crossing between nodal lines and E_F occurs only when M pockets get enlarged [23].

IX. DoS Calculations at the Inter-impurity Site under Various Pairing Scenarios

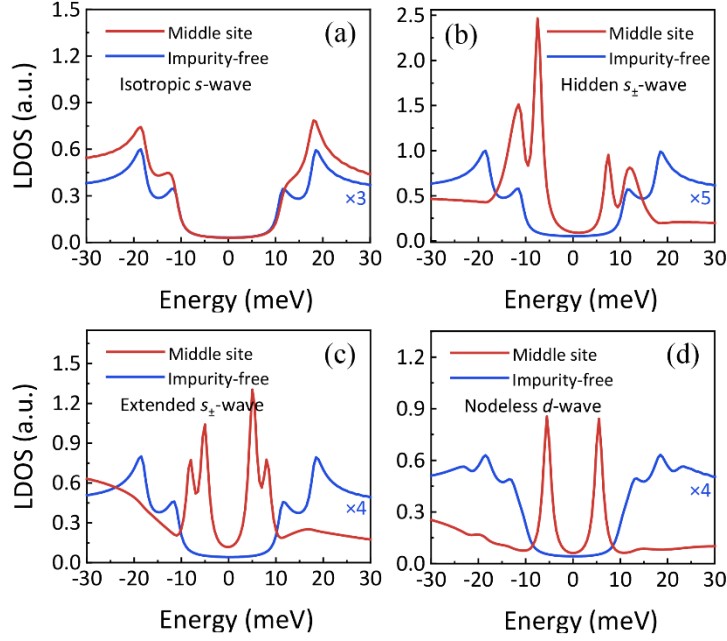


FIG. S14. Calculated DoS upon the middle point of two nonmagnetic impurities at Fe atoms of sublattice A with the location sites of $\mathbf{R}_I = (N/2-2, N/2)$ and $\mathbf{R}_{I'} = (N/2, N/2)$, and for the impurity-free system in (a) isotropic s -, (b) hidden s_{\pm} -, (c) extended s_{\pm} - and (d) nodeless d -wave pairing states, respectively. Here, the strength of the potential scattering: (a) $V_{p,11} = V_{p,22} = 1100$ meV, $V_{p,12} = V_{p,21} = 300$ meV; (b) $V_{p,11} = V_{p,22} = 600$ meV, $V_{p,12} = V_{p,21} = 100$ meV; (c) $V_{p,11} = V_{p,22} = 500$ meV, $V_{p,12} = V_{p,21} = 100$ meV; (d) $V_{p,11} = V_{p,22} = 1700$ meV, $V_{p,12} = V_{p,21} = 1300$ meV.

- [1] Q.-Y. Wang, Z. Li, W.-H. Zhang, Z.-C. Zhang, J.-S. Zhang, W. Li, H. Ding, Y.-B. Ou, P. Deng, K. Chang, J. Wen, C.-L. Song, K. He, J.-F. Jia, S.-H. Ji, Y.-Y. Wang, L.-L. Wang, X. Chen, X.-C. Ma, and Q.-K. Xue, Interface-induced high-temperature superconductivity in single unit-cell FeSe films on SrTiO₃, *Chin. Phys. Lett.* **29**, 037402 (2012).
- [2] C. Liu, Z. Wang, S. Ye, C. Chen, Y. Liu, Q. Wang, Q. H. Wang, and J. Wang, Detection of bosonic mode as a signature of magnetic excitation in one-unit-cell FeSe on SrTiO₃, *Nano Lett.* **19**, 3464–3472 (2019).
- [3] H. Brune, Microscopic view of epitaxial metal growth: nucleation and aggregation, *Surf. Sci. Rep.* **31**, 125 (1998).
- [4] K. Budde, E. Abram, V. Yeh, and M. Tringides, Uniform, self-organized, seven-step height Pb/Si (111)–(7×7) islands at low temperatures, *Phys. Rev. B* **61**, R10602 (2000).
- [5] H. van Kempen, R. Smokers, and P. vanBentum, The Coulomb Blockade in STM-type Tunnel Junctions, *AIP Conf. Proc.* **241**, 101 (1991).
- [6] I. Giaever and H. R. Zeller, Superconductivity of small tin particles measured by tunneling, *Phys. Rev. Lett.* **20**, 1504 (1968).
- [7] L. Geerligs, V. Anderegg, P. Holweg, J. Mooij, H. Pothier, D. Esteve, C. Urbina, and M. Devoret, Frequency-locked turnstile device for single electrons, *Phys. Rev. Lett.* **64**, 2691 (1990).
- [8] T. A. Fulton and G. J. Dolan, Observation of single-electron charging effects in small tunnel junctions, *Phys. Rev. Lett.* **59**, 109 (1987).
- [9] K. Nakazato, R. Blaikie, and H. Ahmed, Single-electron memory, *J. Appl. Phys.* **75**, 5123 (1994).
- [10] D. V. Averin and K. K. Likharev, *Mesoscopic Phenomena in Solids* (Elsevier, Amsterdam, 1991).
- [11] P. Delsing, K. Likharev, L. S. Kuzmin, and T. Claeson, Effect of high-frequency electrodynamic environment on the single-electron tunneling in ultrasmall junctions, *Phys. Rev. Lett.* **63**, 1180 (1989).
- [12] M. H. Devoret, D. Estève, H. Grabert, G.-L. Ingold, H. Pothier, and C. Urbina, Effect of the electromagnetic environment on the Coulomb blockade in ultrasmall tunnel junctions, *Phys. Rev. Lett.* **64**, 1824 (1990).
- [13] A. Hanna and M. Tinkham, Variation of the Coulomb staircase in a two-junction system by fractional electron charge, *Phys. Rev. B* **44**, 5919 (1991).

- [14] Z. Wang, C. Liu, Y. Liu, and J. Wang, High-temperature superconductivity in one-unit-cell FeSe films, *J. Phys.: Condens. Matter* **29**, 153001 (2017).
- [15] W. Wei, Y. Dai, M. Guo, L. Yu, H. Jin, S. Han, and B. Huang, Codoping synergistic effects in N-doped SrTiO₃ for higher energy conversion efficiency, *Phys. Chem. Chem. Phys.* **12**, 7612 (2010).
- [16] Y. Zhu, Y. Dai, W. Wei, and B. Huang, First principles study of Ag-doped, Nb-doped and Ag/Nb doped SrTiO₃, *Rare Metals* **30**, 177 (2011).
- [17] P. Fazekas, *Lecture notes on electron correlation and magnetism* (World Scientific, 1999).
- [18] S. Glass, G. Li, F. Adler, J. Aulbach, A. Fleszar, R. Thomale, W. Hanke, R. Claessen, and J. Schäfer, Triangular Spin-Orbit-Coupled Lattice with Strong Coulomb Correlations: Sn Atoms on a SiC(0001) Substrate, *Phys. Rev. Lett.* **114**, 247602 (2015).
- [19] T. Zhu, W. Ruan, Y.-Q. Wang, H.-Z. Tsai, S. Wang, C. Zhang, T. Wang, F. Liou, K. Watanabe, T. Taniguchi, J. B. Neaton, A. Weber-Bargioni, A. Zettl, Z. Q. Qiu, G. Zhang, F. Wang, J. E. Moore, and M. F. Crommie, Imaging gate-tunable Tomonaga–Luttinger liquids in 1H-MoSe₂ mirror twin boundaries, *Nat. Mater.* **21**, 748 (2021).
- [20] A. L. Efros and B. I. Shklovskii, Coulomb gap and low temperature conductivity of disordered systems, *J. Phys. C: Solid State Phys.* **8**, L49 (1975).
- [21] C. Brun, K. H. Müller, I.-P. Hong, F. Patthey, C. Flindt, and W.-D. Schneider, Dynamical Coulomb blockade observed in nanosized electrical contacts, *Phys. Rev. Lett.* **108**, 126802 (2012).
- [22] Q. Fan, W. H. Zhang, X. Liu, Y. J. Yan, M. Q. Ren, R. Peng, H. C. Xu, B. P. Xie, J. P. Hu, T. Zhang, and D. L. Feng, Plain *s*-wave superconductivity in single-layer FeSe on SrTiO₃ probed by scanning tunnelling microscopy, *Nat. Phys.* **11**, 946 (2015).
- [23] Y. Zhang, J. J. Lee, R. G. Moore, W. Li, M. Yi, M. Hashimoto, D. H. Lu, T. P. Devereaux, D. H. Lee, and Z. X. Shen, Superconducting Gap Anisotropy in Monolayer FeSe Thin Film, *Phys. Rev. Lett.* **117**, 117001 (2016).